UK Atomic Energy Authority

ExCALIBUR

Finite Element Models Complementary Actions 2

M6.2 Version 1.00

Abstract

The report describes work for ExCALIBUR project NEPTUNE at Milestone M6.2. It includes an application of the *Nektar++* finite-element software to the classic problem of vertical natural convection, showing concurrence with numerical results from a benchmark test case in the literature and the replication of some outputs from a recent publication. A further section contains details of a preliminary attempt to explore recent developments in the use of structure-preserving finite-element methods ie. discrete exterior calculus, the vision being that such methods will enable finite-element outputs to integrate reliably with developments in particle-based codes within NEPTUNE.

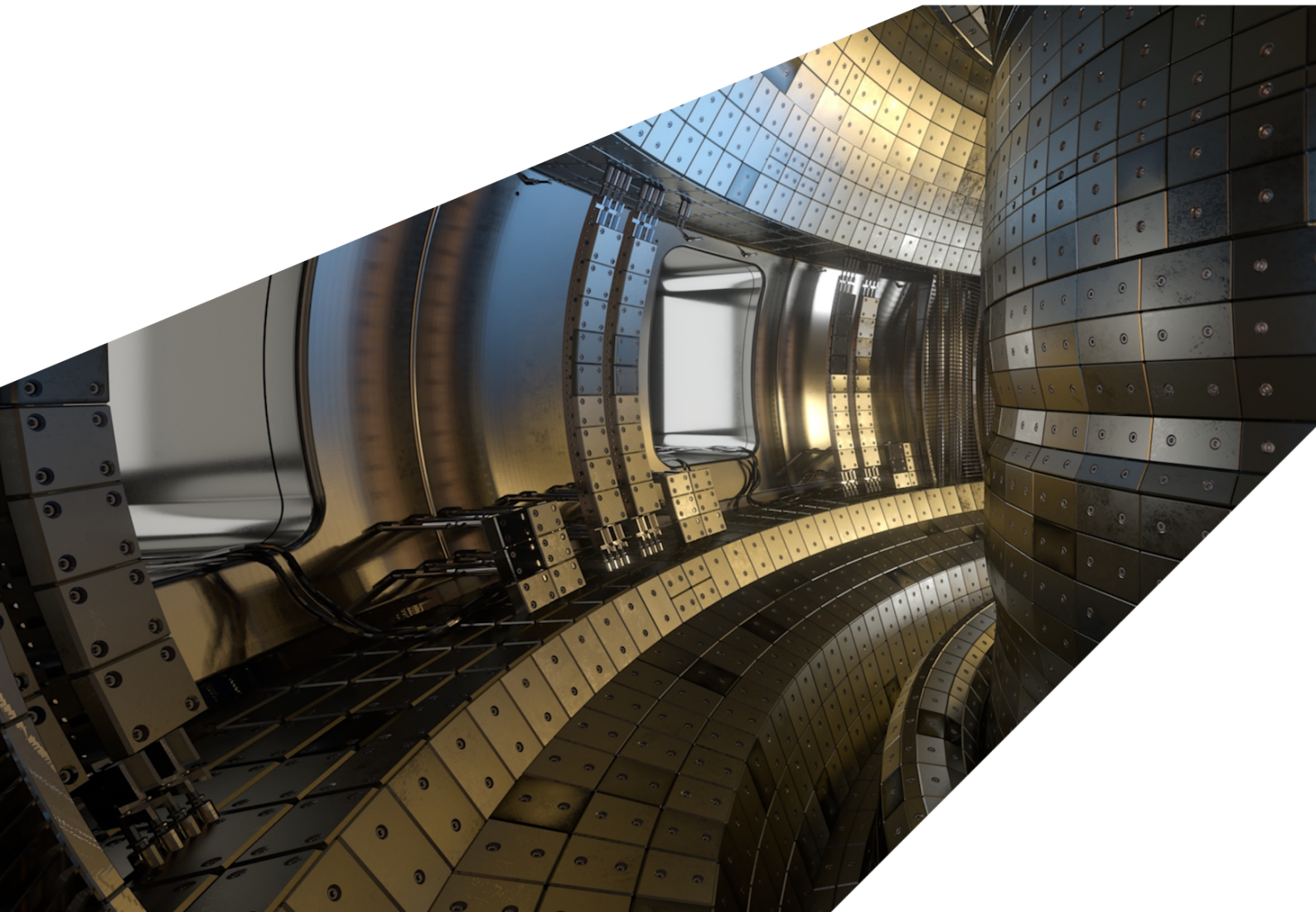

UKAEA REFERENCE AND APPROVAL SHEET

	Client Reference:	
	UKAEA Reference:	CD/EXCALIBUR-FMS/0064
	Issue:	1.00
	Date:	18 March 2022
Project Name: ExCALIBUR Fusion Modelling System		

	Name and Department	Signature	Date
Prepared By:	Ed Threlfall BD	N/A	18 March 2022
Reviewed By:	Wayne Arter Project Technical Lead	W. Arter	18 March 2022

1 Introduction

High-order methods, which offer the potential for exponential improvement in accuracy given polynomial increase in computation time, are seen as essential for maximizing the performance of next-generation software intended to run on forthcoming exascale machines. One specific example of such an approach is the spectral / hp finite element method [1], of which a modern, open-source C++ implementation is the software *Nektar++* [2] co-written and maintained by one of the NEPTUNE grantees. The *Nektar++* framework forms the basis for some of the core NEPTUNE proxyapps and is currently being augmented with capabilities to handle fusion-relevant problems ([3], [4]) and also extension to allow optimized operation on a wider range of computational architectures. This involvement justifies continued investment of UKAEA time in verification and validation of the framework, e.g. by comparison to published results, and, with a view to future extensions, in understanding its operation. In view of its overarching focus on finite-element methods, this deliverable relates primarily to Work Package FM-WP1 - Numerical Representation.

In Section 2, a comparison between *Nektar++* outputs and a well-known benchmark result for convective heat transfer is performed, and also some results from a recent paper on convection modelling are replicated. This work extends fluid methods studied in the prequel [5] in terms of comparison to results from the literature.

The simulation of the plasma edge will require models going beyond the purely fluid-mechanical treatment in 2 in order to describe the physics in regions where collisionality is low. This kinetic regime can be accessed by the use of particle methods, which literally attempt an atomistic dynamical simulation (though each computational particle may correspond to very many physical particles). The current wisdom associated to the coupling of particles to continuum fields (e.g. electromagnetism) harbingers deeper changes to the existing *Nektar++* framework. Specifically, numerical properties of the coupled particle-field solver are known to benefit greatly, for example in terms of stability guarantees, from the use of structure-preserving methods, in which aspects of the continuum physics survive the transition to a discrete representation. These techniques go also under the name of ‘discrete exterior calculus’ or ‘finite-element exterior calculus’ as they preserve some of the attributes of continuum exterior calculus. As a prelude to these expected changes, a brief exposition of such a translation is given in Section 3 for a simple toy problem using a method taken from the literature; the example is shown to achieve spectral convergence (via the use of a small stand-alone code).

The test problems treated herein are sufficiently small so as not to benefit much from execution on HPC hardware, and the results were obtained using only a modest desktop PC. The at-scale capability of the *Nektar++* framework is the subject of current study and future work by the developers of that code and is beyond the ambit of this report.

2 Vertical natural convection in *Nektar++*

2.1 Introduction

This work follows-on from the investigation described in the previous report [5], which treated the problem of heat transport in vertical natural convection (for an illustration of the relevance of such problems to the fusion use case, see [6]). One new aspect of the current work is the replication of numerical results published in the literature.

In vertical natural convection an upright cavity has a hot side and a cold side and is filled with a fluid that experiences a vertical buoyancy force when heated. The strength of this force then leads to different regimes of flow and heat transport. When the force is negligible, heat is transferred diffusively from the hot surface to the cold one, in rough analogy with classical transport. Greater buoyancy leads to fluid moving up the hot side, across the top of the cell, and down the cold side, creating a steady (laminar, or 'classical') circulation and transporting heat by advection. As the force is increased, the vertical flow becomes increasingly confined to a velocity boundary layer near the vertical walls; likewise, the temperature gradients are increasingly restricted to a thermal boundary layer near the vertical walls. Further increasing the force, one finds that the sheared flow near the vertical boundaries leads to an instability of Kelvin-Helmholtz type that takes the form of waves that co-move with the convective flow, and which are chaotic in nature; these boundary effects also lead ultimately to complicated, also-chaotic, time-dependent flow structures in the bulk - turbulent flow. As in the previous report, the simulations are two dimensional and thus truly three-dimensional effects - including expected instabilities - are excluded *a priori*.

In dimensionless form, the system of equations describing vertical natural convection is, for fluid velocity $\mathbf{u}$, temperature T and pressure p, for a system coordinatized such that the vertical, gravity-opposing direction is $\hat{\mathbf{y}}$,

$$\frac{1}{Pr}\left(\frac{\partial \mathbf{u}}{\partial t} + \mathbf{u}\cdot\nabla\mathbf{u}\right) = -\nabla p + Ra\, T\, \hat{\mathbf{y}} + \nabla^2\mathbf{u}, \tag{1}$$

$$\left(\frac{\partial T}{\partial t} + \mathbf{u}\cdot\nabla T\right) = \nabla^2 T, \tag{2}$$

$$\nabla\cdot\mathbf{u} = 0. \tag{3}$$

The Boussinesq approximation is assumed, with the density fluctuation entering only as a temperature-dependent buoyancy force (hence the incompressibility condition) - for this reason, the system is simulated using the incompressible Navier-Stokes solver of *Nektar++*. Dirichlet boundary conditions were used for the vertical wall temperatures ($T = 1$ on the left and $T = 0$ on the right) and zero Neumann conditions (i.e. no heat flux) on the horizontal walls (top and bottom). The velocity boundary conditions were no-slip / no-penetration and the pressure used a zero Neumann condition, for all walls.

The dimensionless parameters are the Rayleigh number, where β is the thermal expansion coefficient, ΔT the temperature difference across cavity width L,

$$Ra = \frac{\beta g \Delta T L^3}{\kappa \nu} \tag{4}$$

and the Prandtl number: the ratio of kinematic viscosity ν to thermal diffusivity κ (a property of the fluid filling the cavity; in these simulations, the value 0.71, appropriate to air, was used),

$$Pr = \frac{\nu}{\kappa} \, . \tag{5}$$

The other relevant parameter is the aspect ratio $\lambda = L/H$ of the cavity (width L, height H).

The heat flux the spatial-averaged Nusselt number defined as

$$Nu = \frac{\int_0^H -\partial/\partial x T(x_0, y) + \partial/\partial x T(x_1, y) dy}{\int_0^H -\partial/\partial x T(x_0, y) + \partial/\partial x T(x_1, y) dy|_{Ra=0}} \, . \tag{6}$$

Computational parameters enter as the mesh resolution (for simplicity, meshes comprising uniform squares are used for this study, with h denoting the size of a single element) and the global order p (a natural number) of the spectral elements, with the lowest allowed value ($p = 1$) meaning that linear intra-element basis functions are used, and greater p corresponding to higher-order Lagrange polynomials. For reference, a continuous Galerkin formulation was employed.

2.2 New numerical results

Verification of the incompressible Navier-Stokes solver of *Nektar++* was performed for the case of two convective flows. The first of these, which will be the main focus, is identical to the MIT benchmark [7] and uses a Rayleigh number Ra of 3.4×10^5, giving a steady flow with a time-periodic flow instability. The second differs only in using a larger value of Ra, 5.5×10^5, at which the flow instability is no longer periodic (see Figs. 1 and 2), probably due to the operation of multiple linear instability modes of incommensurate period. The setup involves a computational domain with aspect ratio $8:1$ i.e. a tall narrow tank of fluid. The MIT benchmark was established in order to identify the time-dependent solution for the cavity described above, to find the critical Rayleigh number for the onset of flow instability, and to identify computational methods capable of providing these results. Two of the quantities of interest in the study are the time-averaged, spatially-averaged Nusselt number and the time series of the temperature at the point $(x, y) = (0.181, 7.37)$. The former is presented in a table of results obtained by various authors, while the latter is available for download, both at [7].

A uniform grid of 800 $p = 10$ spectral elements was used, unlike the MIT benchmark which uses computational meshes that are refined near the boundaries to better resolve the boundary layers (note that the paper [8], which appears to use a uniform mesh, contains evidence that the resolution used herein is sufficient to resolve relevant physics of both flows). Timestep sizes were set (by trial-and-error) to be close to but not in violation of the stability limit on the maximum allowed timestep. Regarding computational resources, the simulations are not particularly onerous, with

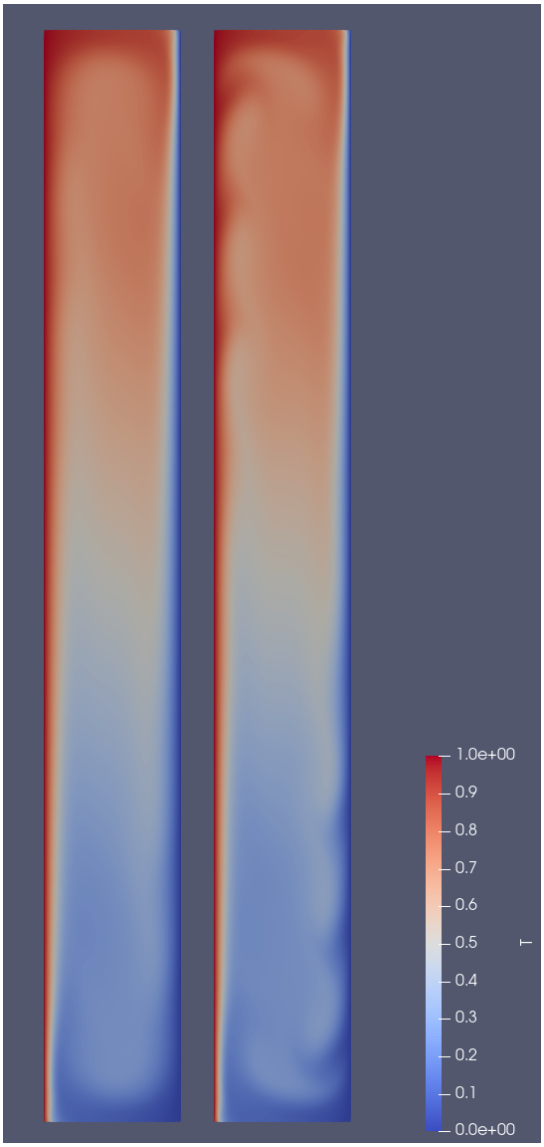

Figure 1: Temperature fields for Ra of 3.4×10^5 (left) and 5.5×10^5 (right). Note the appearance of the 'wall waves' in the larger-Ra case, in which the steady configuration is replaced by a time-dependent quasi-steady state.

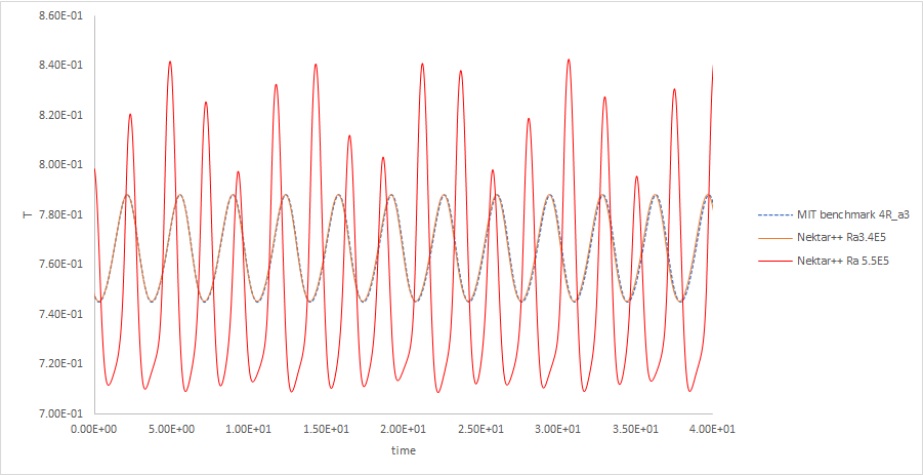

Figure 2: Field-at-point outputs showing Nektar++ and MIT benchmark data. Temperature field recorded at point '1' described in [7] i.e. $(x, y) = (0.181, 7.37)$. Note absence of periodicity of the flow instability in the higher-Ra case.

ten periods of the lower-Ra example taking approx. 30mins to run on a single Core-i7-10700KF 3.8GHz PC (the higher-Ra case is somewhat slower due to the use of a smaller timestep).

The Nusselt number was computed as a time series using a customized *Nektar++* filter, described in [5] and representing the sole modification of the existing code base for the work described in this section. The mean value of the time series data was evaluated as the average of the maximum and minimum of the time series (using a small timestep for all simulations meant that this approach was sufficiently accurate).

The most accurate of the Nusselt number results reported in [7] for the $Ra = 3.4 \times 10^5$ flow appears to be that obtained by le Quéré, with a value of 4.57946. This is 0.002% different from the converged value obtained from *Nektar++* and presented in the table 1 (note these results all used the same timestep size). This level of agreement falls slightly short of the exact (to 6 sf) concurrence shown in [8] - this minor discrepancy may be down to details of the solver implementation, or perhaps the method used for the time-averaging. The value of the time-averaged Nusselt number obtained from *Nektar++* can also be seen, in the figure 4, to converge spectrally with the element order p. Note also the wall-clock run times tabulated in Table 1, which indicate that the computation is not bound by arithmetic; the number of degrees of freedom scales as $(p + 1)^2$ and these execution times obviously do not scale even nearly as strongly as p^2.

Good agreement with the point temperature was also obtained for the lower Ra-value case (Fig.2), in which the MIT benchmark data is available for download from [7] - amplitude and period can be seen to match. The higher-Ra value generates a time series that is chaotic and thus the comparison is less straightforward since only its statistical properties can meaningfully be compared (not done here).

The lower-Ra simulation contains a periodic perturbation, the flow field of which can be visualized and compared to Figs.5-7 of [8]. Excellent visual agreement with those figures is obtained in *Nektar++* outputs (note the amplitude of the perturbation is not meaningful as the phase is not quoted

Element order p	time-av. Nusselt number Nu	Execution time / s (16 logical cores)
1	3.66566	38
2	4.95898	97
3	4.62167	171
4	4.54045	336
5	4.56850	601
6	4.57956	799
7	4.57977	1047
8	4.57943	1627
9	4.57936	1903
10	4.57935	2466
11	4.57935	3029

Table 1: Table of time-averaged Nusselt number values for $Ra = 3.4 \times 10^5$ obtained from *Nektar++*.

in the paper). The procedure for extracting these plots from *Nektar++* involves identification of the time-dependent parts of the solution (see e.g. Fig.5 of [8]) in a relatively large-amplitude steady-state background - the laminar convective cell - which needs to be subtracted. This is done using the Nektar++ time-averaged field filter to compute the time-averaged background field, and then processing the outputs to subtract the background using the *FieldConvert* postprocessing utility of *Nektar++* (the command is `fieldconvert -m addfld:fromfld=MIT_Ra_3pt4e5_averaged.fld:scale=-1 MIT_Ra_3pt4e5.xml MIT_Ra_3pt4e5.fld MIT_Ra_3pt4e5_fluctuation.fld`) (See Fig.3 for Nektar++ output).

Note a couple of points: the Nektar++ simulations use a differently-scaled time variable: to convert from that used in Nektar++ to that used in [8] and [7], multiply by $\sqrt{RaPr}$ (Pr is the Prandtl number, 0.71 for both cases). Also note that [7] uses a temperature of 0.5 on the hot side and -0.5 on the cold side, while [8] and the Nektar++ files use values of 1 and 0 respectively - conversion trivial.

In summary, very good agreement between published results and *Nektar++* simulation results is shown for averaged Nusselt numbers computed close to but on either side of the critical Rayleigh number, and linear perturbations to flow-field profiles in time and space just beneath the critical value of the Rayleigh number. Note that these Rayleigh number values fall rather short of resulting in a truly turbulent overall flow of the sort reported in [5].

3 Preliminary study of discrete exterior calculus

3.1 Introduction

In recent years, structure-preserving methods have been applied to finite-element methods. In short, these techniques ensure that certain important properties of the continuum system (e.g. local conservation laws) are preserved in the discretized version (i.e. the action of discretization commutes with certain operations, such as forming curls or divergences). There is a growing literature on the advantages of such methods as relevant to e.g. stability and charge conservation

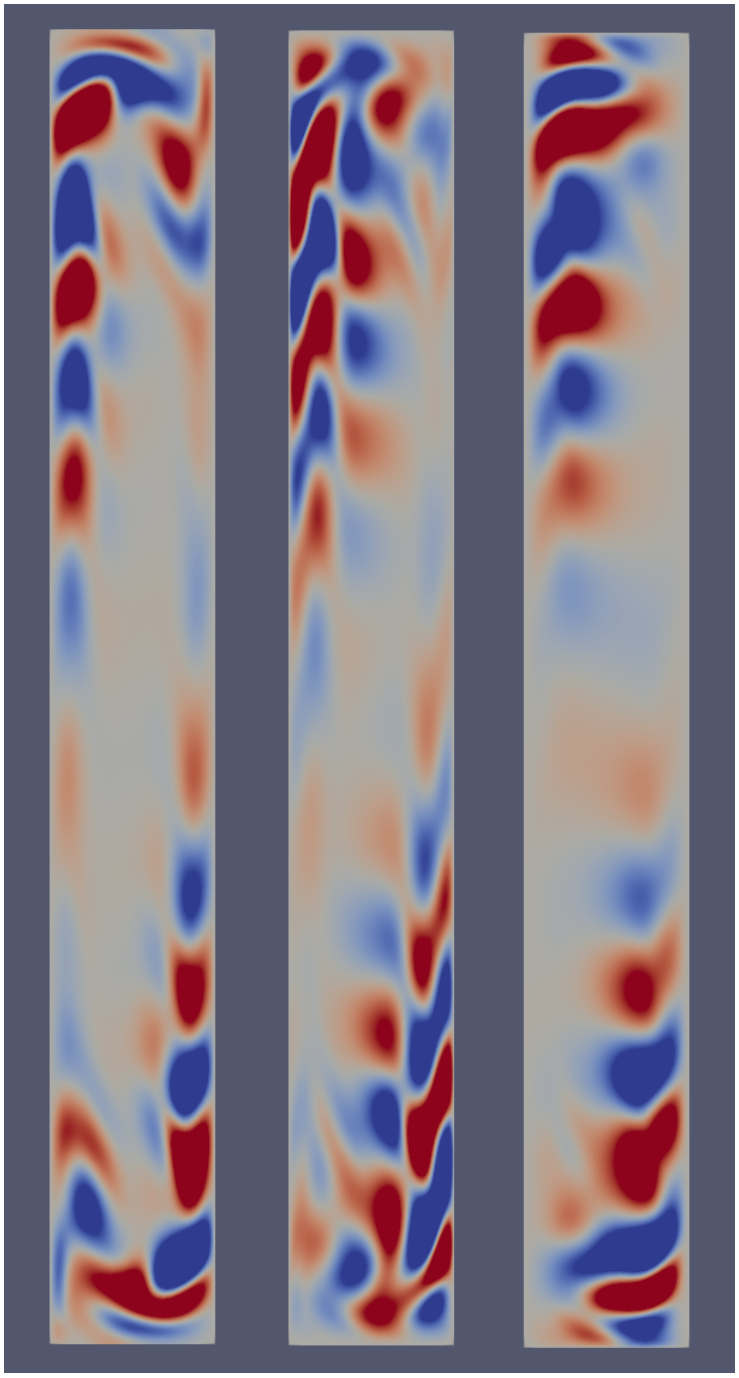

Figure 3: Nektar++ fluctuation fields for T, v, u (respectively temperature, vertical velocity, horizontal velocity), corresponding to Figs.5-7 of [8], computed by subtracting fields averaged over one period of $Ra = 3.4 \times 10^5$ case. Scales are excluded as phase does not correspond to that used in figures from the reference.

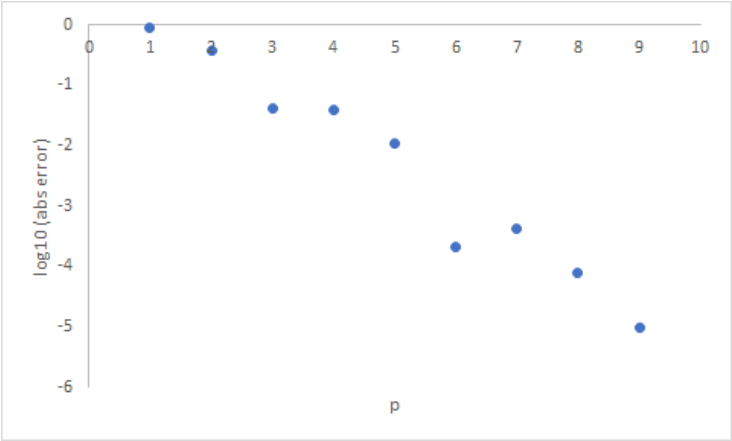

Figure 4: Demonstration of spectral convergence for the Nusselt numbers displayed in Table 1.

[9], often using a discretization of Whitney type [10, 11, 12].

Complete understanding of the literature on this subject is something of a challenge for the non-specialist; however, a clear presentation can be found in [13] for the case of a globally-spectral implementation of discrete exterior calculus. The formalism there described is here used to treat a simple toy problem, allowing a transparent, elementary presentation of the recipe including such relevant actors as the mesh, discrete exterior derivative operator, and discrete Hodge star - and the duals of all three of the aforementioned. The reference [13] should be consulted for details of various attractive properties that make the formulation work as the presentation here concerns itself only with the basics.

3.2 A simple problem solved using discrete exterior calculus

The problem treated is a one-dimensional ordinary differential equation of Helmholtz type,

$$\frac{d^2u(x)}{dx^2} + \frac{u(x)}{\pi} = f(x). \tag{7}$$

The domain of interest is taken to be the interval $[0, 2\pi]$ with a periodic boundary condition. It is clear that the choice of a periodic domain avoids complications with what to do with the mesh and dual mesh at the end points.

In exterior calculus language, the equation is expressed as

$$*\, d * du + \frac{u}{\pi} = f \tag{8}$$

for 0-forms u and f, exterior derivative d and Hodge star $*$. The composite $*d*d$ is referred to as the Laplace-Beltrami operator in the literature (in this simple case it represents the Laplacian operating on a scalar).

It is clear that the equation is self-consistent in the pattern of forms, i.e. u is a 0-form, du a 1-form, $*du$ a 0-form, and so forth.

The basis functions taken from [13] are

$$\alpha_N(x) = \frac{1}{N} \begin{cases} \cot \frac{x}{2} \sin \frac{Nx}{2} \text{ (N even)} \\ \operatorname{cosec} \frac{x}{2} \sin \frac{Nx}{2} \text{ (N odd)} \end{cases} \tag{9}$$

$$\beta_N(x) = \begin{cases} \frac{1}{2\pi} - \frac{1}{4} \cos \frac{Nx}{2} + \frac{1}{N} \sum_{n=1}^{\frac{N}{2}} \frac{n \cos nx}{\sin n\pi N} \text{ (N even)} \\ \frac{1}{2\pi} \sum_{n=1}^{\frac{N-1}{2}} \frac{n \cos nx}{\sin n\pi N} \text{ (N odd)} \end{cases} \tag{10}$$

Further definitions are $\alpha_{N,n}(x) \equiv \alpha_N(x - nh)$ and $\beta_{N,n}(x) \equiv \beta_N(x - nh)$, for $h \equiv 2\pi N$.

Note that these functions have the properties $\alpha_{N,n}(x_m) = \delta_{mn}$ and $\int_{x_m - \frac{h}{2}}^{x_m + \frac{h}{2}} \beta_{N,n}(x) dx = \delta_{mn}$.

The basis functions for the primal forms, defined on a primal mesh of N evenly-spaced nodes in the interval $[0, 2\pi]$, are then

$$\phi^0_{N,n}(x) = \alpha_{N,n}(x) \tag{11}$$

and

$$\phi^1_{N,n}(x) = \beta_{N,n+\frac{1}{2}}(x)\ dx. \tag{12}$$

The corresponding dual forms, described on the Voronoi dual mesh which has nodes half-way between those of the primal mesh, are

$$\tilde{\phi}^0_{N,n}(x) = \alpha_{N,n+\frac{1}{2}}(x) \tag{13}$$

(noting that a tilde is used to denote a dual quantity in the discrete representation) and

$$\tilde{\phi}^1_{N,n}(x) = \beta_{N,n}(x)\ dx. \tag{14}$$

Examination of the equation 8 makes it clear that an expression for the discrete Hodge star acting on a 1-form is required. This is obtained from

$$H^k_{ij} = \int_{\tilde{\sigma}^{n-k}_i} *\phi^k_j, \tag{15}$$

and for the dual Hodge star operator

$$\tilde{H}^k_{ij} = \int_{\sigma^{n-k}_i} *\tilde{\phi}^k_j, \tag{16}$$

with $n = 1$ and $k = 1$ in both cases (note that in this problem, the α functions are used only to plot the solution, and the β functions are only used in evaluating the discrete Hodge operators).

The final pieces are the discrete exterior derivative operators on the primal and dual meshes. These have the expected form though one subtlety is that the primal mesh operator is a forward difference while the dual is a backward difference; explicitly, in a small example ($N = 4$)

$$D = \begin{pmatrix} -1 & 1 & 0 & 0 \\ 0 & -1 & 1 & 0 \\ 0 & 0 & -1 & 1 \\ 1 & 0 & 0 & -1 \end{pmatrix} \tag{17}$$

for the primal and

$$\tilde{D} = \begin{pmatrix} 1 & 0 & 0 & -1 \\ -1 & 1 & 0 & 0 \\ 0 & -1 & 1 & 0 \\ 0 & 0 & -1 & 1 \end{pmatrix} \tag{18}$$

for the dual.

Having assembled these matrices, the method can be applied and tested. The matrix equation is

$$\tilde{H}^1 \tilde{D} H^1 D \underline{u} + \frac{1}{\pi} \underline{u} = \underline{f}. \tag{19}$$

The matrix multiplication and inversion routines included in Intel Math Kernel Library (MKL) [14] were used; the system is small enough that a direct solver, based on a LU decomposition, is effective. Note that the inclusion of the reaction term $\frac{u}{\pi}$ in the equation removes from the complementary function a constant term and a general solution with periodicity 2π (were this not the case, the matrix obtained would be expected to be singular); this difficulty can also be avoided by abandoning the periodic boundary condition. Analytic solutions of the differential equation 7 are easily generated using the method of manufactured solutions, in this case by evaluating the right-hand-side ($f(x)$) corresponding to the periodic solution $u = e^{3 \sin 2x}$. A graph of the convergence with N of the resulting numerical problem is shown in Fig. 5. Note the $L_{\inf}$ error (assessed against the analytic solution) was used as the basis for this assessment, as is the case in [13]. The exponential convergence seen here can be compared to that obtained by more elementary approaches such as second-order finite-difference for which the convergence would be polynomial (error $\propto h^2$).

In conclusion, a spectral method using the machinery of discrete exterior calculus has been described and used to solve a simple problem. These methods have much potential for solving more interesting systems, potential that is achieved at the expense of more involved mathematics than that outlined here. It is anticipated that the implementation chosen for NEPTUNE will be a spectral / hp method rather than the globally-spectral method illustrated here.

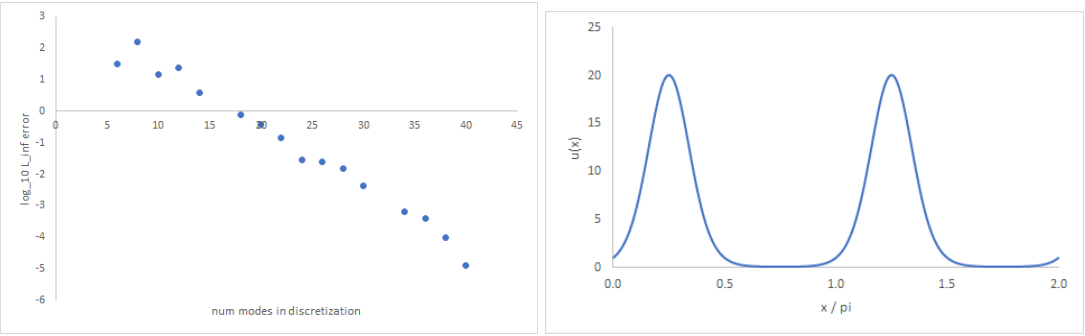

Figure 5: Exponential convergence of the discrete exterior calculus implementation explained in the main text (left). Solution curve for $N = 40$ shown to right.

4 Summary

This report has provided further numerical results using the *Nektar++* framework, continuing investigations started in [5]. Explicit numerical agreement between *Nektar++* simulations of vertical natural convection and corresponding results from the literature was demonstrated.

Additionally, a simple application of discrete exterior calculus to a toy problem, exhibiting spectral convergence, was shown using a simple code written by the author. It is apparent that the extension of the *Nektar++* framework to support less elementary implementations will entail a significant amount of effort in order to understand the theory of higher-order discrete exterior calculus and to incorporate this within the framework in a modular and sustainable way.

The author would like to thank the developers of *Nektar++* for useful discussions.

Acknowledgement

The support of the UK Meteorological Office and Strategic Priorities Fund is acknowledged.

References

[1] G. Karniadakis and S. Sherwin. *Spectral/hp element methods for computational fluid dynamics 2nd Ed.* Oxford University Press, 2005. https://doi.org/10.1093/acprof:oso/9780198528692.001.0001.

[2] D. Moxey et al. Nektar++ website. https://www.nektar.info, 2020. Accessed: June 2020.

[3] Nektar-diffusion proxyapp. https://github.com/ExCALIBUR-NEPTUNE/nektar-diffusion, 2021. Accessed: September 2021.

[4] Nektar++ solver for Hasegawa-Wakatani equations. https://github.com/ExCALIBUR-NEPTUNE/nektar-driftwave, 2021. Accessed: September 2021.

[5] E. Threlfall and W. Arter. Finite Element Models: Complementary Activities I. Technical Report CD/EXCALIBUR-FMS/0051-M6.1, UKAEA, 2021. https://github.com/ExCALIBUR-NEPTUNE/Documents/blob/main/reports/ukaea_reports/CD-EXCALIBUR-FMS0051-M6.1.pdf.

[6] F. Wilczynski, D.W. Hughes, S. Van Loo, W. Arter, and F. Militello. Stability of scrape-off layer plasma: A modified Rayleigh–Bénard problem. *Physics of Plasmas*, 26(2):022510, 2019. https://doi.org/10.1063/1.5064765.

[7] MIT Benchmark. http://www.mathematik.tu-dortmund.de/~featflow/en/benchmarks/cfdbenchmarking/mit_benchmark.html. Accessed: March 2022.

[8] V. Zucatti, H.F.S. Lui, D.B. Pitz, and W.R. Wolf. Assessment of reduced-order modeling strategies for convective heat transfer. *Numerical Heat Transfer: Part A: Applications 77:7*, pages 702–729, 2020.

[9] S. O'Connor, Z.D. Crawford, and O.H. Ramachandran. Time-integrator-agnostic charge-conserving finite-element PIC. *Phys. Plasmas* **28***, 09211;* `https://doi.org/10.1063/5.0046842`, 2021.

[10] L. Kettunen, J. Lohi, J. Räbinä, S. Mönkölä, and T. Rossi. Generalized finite-difference schemes with higher-order Whitney forms. *ESAIM Mathematical Modelling and Numerical Analysis,* **55**, pages 1439–1460, 2021.

[11] F. Rapetti. High-order edge elements on simplicial meshes. *ESAIM Mathematical Modelling and Numerical Analysis,* **41**, pages 1001–1020, 2007.

[12] F. Rapetti and A. Bossavit. Whitney forms of higher degree. *SIAM Journal on Numerical Analysis Vol.47, Iss.3 10.1137/070705489*, 2009.

[13] D.S. Rufat. Spectral exterior calculus and its implementation. *PhD thesis, Caltech*, 2017.

[14] Intel oneAPI Math Kernel Library. `https://www.intel.com/content/www/us/en/develop/documentation/get-started-with-mkl-for-dpcpp/top.html`, 2022. Accessed: March 2022.